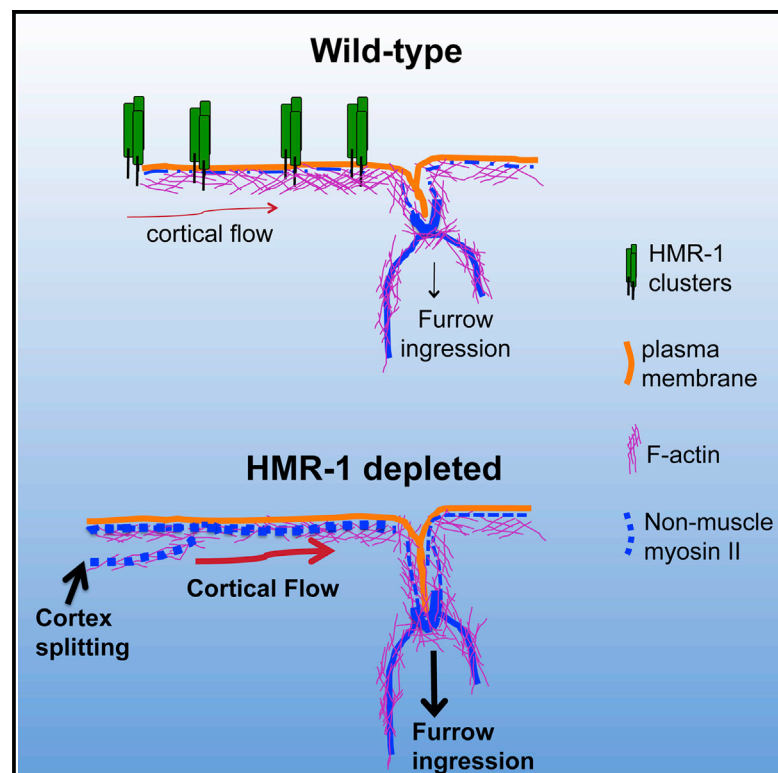


Current Biology

Non-junctional E-Cadherin Clusters Regulate the Actomyosin Cortex in the *C. elegans* Zygote

Graphical Abstract



Authors

Anup Padmanabhan, Hui Ting Ong,
Ronen Zaidel-Bar

Correspondence

biezbr@nus.edu.sg

In Brief

Padmanabhan et al. discover a non-canonical role for E-cadherin that is independent of cell adhesion. In the *C. elegans* zygote, non-junctional E-cadherin clusters inhibit formin and myosin activity, stabilize the cortex, and resist its flow. In the absence of E-cadherin, cytokinetic furrow ingression is faster, but the cortex may split in two.

Highlights

- Non-junctional E-cadherin clusters associate with cortical actin in *C. elegans* embryos
- E-cadherin clusters resist cortical flow and inhibit RhoA and myosin II localization
- E-cadherin depletion in *C. elegans* zygotes accelerates cytokinetic furrow ingression
- E-cadherin supports structural integrity of the cell cortex independent of cell adhesion



Non-junctional E-Cadherin Clusters Regulate the Actomyosin Cortex in the *C. elegans* Zygote

Anup Padmanabhan,¹ Hui Ting Ong,¹ and Ronen Zaidel-Bar^{1,2,3,*}¹Mechanobiology Institute, National University of Singapore, 5A Engineering Drive 1, Singapore 117411, Singapore²Department of Biomedical Engineering, National University of Singapore, 4 Engineering Drive 3, Singapore 117583, Singapore³Lead Contact*Correspondence: biezbr@nus.edu.sg<http://dx.doi.org/10.1016/j.cub.2016.10.032>

SUMMARY

Classical cadherins are well known for their essential function in mediating cell-cell adhesion via their extra-cellular cadherin domains and intra-cellular connections to the actin cytoskeleton [1–3]. There is evidence, however, of adhesion-independent cadherin clusters existing outside of cell-cell junctions [4–6]. What function, if any, these clusters have is not known. HMR-1, the sole classical cadherin in *Caenorhabditis elegans*, plays essential roles during gastrulation, blastomere polarity establishment, and epidermal morphogenesis [7–11]. To elucidate the physiological roles of non-junctional cadherin, we analyzed HMR-1 in the *C. elegans* zygote, which is devoid of neighbors. We show that non-junctional clusters of HMR-1 form during the one-cell polarization stage and associate with F-actin at the cortex during episodes of cortical flow. Non-junctional HMR-1 clusters downregulate RHO-1 activity and inhibit accumulation of non-muscle myosin II (NMY-2) at the anterior cortex. We found that HMR-1 clusters impede cortical flows and play a role in preserving the integrity of the actomyosin cortex, preventing it from splitting in two. Importantly, we uncovered an inverse relationship between the amount of HMR-1 at the cell surface and the rate of cytokinesis. The effect of HMR-1 clusters on cytokinesis is independent of their effect on NMY-2 levels, and is also independent of their extra-cellular domains. Thus, in addition to their canonical role in inter-cellular adhesion, HMR-1 clusters regulate RHO-1 activity and NMY-2 level at the cell surface, reinforce the stability of the actomyosin cortex, and resist its movement to influence cell-shape dynamics.

RESULTS AND DISCUSSION

Adhesion-Independent HMR-1 Clusters Assemble at Contact-free Cell Surfaces

To understand the role of HMR-1 in early embryos, we utilized a functional fusion of HMR-1 with GFP to follow its localization and

dynamics. Immediately after fertilization, HMR-1 was observed as diffuse patches all over the cell surface. During polarization, HMR-1 patches coalesced into dense clusters ($0.61 \pm 0.08 \mu\text{m}^2$; $N = 240$) that concentrated at the anterior half of the embryo (Figures 1A and S1A; Movie S1). Co-labeling with a plasma membrane marker confirmed the clusters to be localized at the cell surface. Both individual clusters and overall HMR-1::GFP levels at the surface appeared to be stable over the time course of our imaging (>500 s) (Figures S1A and S1B; Movie S2). Upon initiation of cytokinesis, HMR-1::GFP clusters displayed rapid rotational movement (Figure 1B, top; Figure S1C; Movie S2, from time 1,000 s to the end). This rotational movement was dependent on actomyosin cortical contractility [12], as inhibition of non-muscle myosin II (NMY-2) activity (by upshifting the temperature-sensitive mutant *nmy-2(ne3409)* [13] to 20°C) abolished the strong rotational movement of HMR-1 clusters (Figure 1B, bottom; Figure S1D). Following cell division, a subset of HMR-1 congregated at the newly formed cell-cell interface, but non-junctional HMR-1 clusters were still observed in two-cell- and four-cell-stage embryos (Figure 1A). Non-junctional HMR-1 clusters could also be observed in immunostaining of endogenous HMR-1 [14].

HMR-1 Association with F-actin Increases during Cortical Flows

E-cadherin at cell-cell junctions has been shown to associate with filamentous actin (F-actin) [15]. Therefore, we examined the relationship between non-junctional HMR-1 clusters and F-actin labeled by Lifeact tagged with red fluorescent protein (RFP). During the polarity maintenance phase, we observed limited lateral association between HMR-1::GFP clusters and F-actin (mean Pearson's coefficient of correlation [PCC] = -0.03 ± 0.06 ; $n = 103$) (Figures 1C and 1D). A significant increase in this association was observed during phases of cortical flow, specifically during polarization (mean PCC = $+0.43 \pm 0.07$; $n = 120$) and the cortical rotation accompanying cytokinesis initiation (mean PCC = $+0.41 \pm 0.07$; $n = 118$) (Figures 1C and 1D), suggesting that as the cortex flows, HMR-1 clusters are being swept along by moving F-actin cables. Consistently, time-lapse movies demonstrated simultaneous transport of HMR-1 clusters and F-actin bundles and instances in which HMR-1 clusters are overtaken by faster-moving F-actin (Figure 1E, frames 7 and 8). Consistent with this notion, particle image velocimetry (PIV) analysis of the cytokinesis-associated cortical rotation showed that the mean $|V_Y|_{\text{max}}$ of HMR-1 clusters ($0.33 \pm 0.07 \mu\text{m/s}$; $n = 14$ embryos) was significantly slower than that of cortical F-actin flow ($0.43 \pm 0.07 \mu\text{m/s}$; $n = 14$ embryos) (Figure 1F).

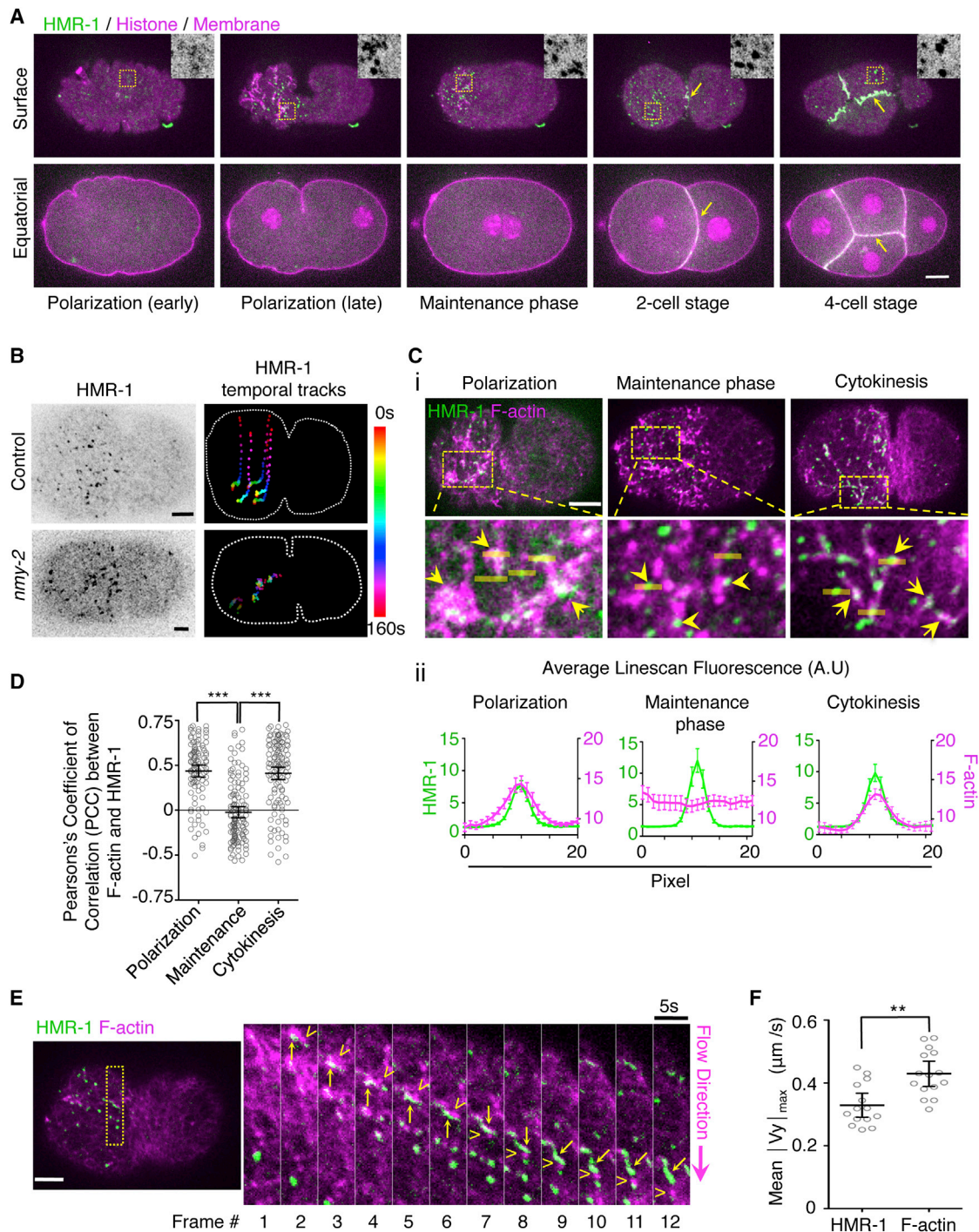


Figure 1. Non-junctional HMR-1 Clusters Assemble during Polarization and Show Increased Association with F-Actin during Cortical Actomyosin Flows

(A) Cell-surface (top) and equatorial (bottom) views of one-cell-, two-cell-, and four-cell-stage embryos co-expressing HMR-1::GFP, mCherry::PLC1 δ -PH, and Histone::mCherry. Insets: the GFP channel from the yellow region of interest (ROI) shows a disperse cloud of HMR-1::GFP assembling into well-defined clusters at the contact-free surface. Arrows indicate junctional HMR-1::GFP at the inter-cellular boundary.

(B) Color-coded temporal tracks highlight the trajectory of a subset of HMR-1 clusters during the initial phase of cytokinesis. Rotational movement of HMR-1 clusters is strongly attenuated upon loss of myosin contractility (ts mutant *nmy-2(ne3409)*).

(C) (i) Cortical views of embryos co-expressing HMR-1::GFP and Lifeact::RFP showing association between F-actin and HMR-1 clusters during polarization (left, arrows), maintenance phase (center, arrowheads), and cytokinesis (right, arrows). Line scans are denoted as yellow lines in the enlarged ROIs. (ii) Average two-color intensity line scans show increased spatial co-localization during stages of cortical flow. From ten embryos, 103 line scans were analyzed during polarization, 120 during the maintenance phase, and 118 during cytokinesis-associated cortical rotation. Error bars are mean \pm SEM.

(legend continued on next page)

Non-junctional HMR-1 Clusters Inhibit Cortical NMY-2

The cortex of early *Caenorhabditis elegans* embryos is composed of dense foci of NMY-2 interconnected by F-actin bundles forming an actomyosin meshwork [14, 16]. Cortical flows, driven by NMY-2-based contractility [14, 17], generate embryonic polarity when directed from the posterior to the anterior [14, 18] and chirality when the flow is rotational [17]. To determine the relationship between HMR-1 clusters and NMY-2 foci, we imaged transgenic embryos expressing HMR-1::GFP and NMY-2::mCherry during the polarity maintenance phase and found their localization at the cortex to be mutually exclusive (Figure 2A). Likewise, during cytokinesis, the medial contractile zone was enriched in NMY-2 driving furrow ingression, but HMR-1 was largely absent from this region (Figure 2B). HMR-1 accumulated only after NMY-2 levels diminished, once cytokinesis was completed (Figure 2C). This mutually exclusive localization suggested an antagonism between HMR-1 and NMY-2 at the cortex. To test this idea, we depleted HMR-1 by RNAi and measured the levels of NMY-2::GFP at the cell surface as well as at the ingression furrow of the first dividing cell (Figure 2D). NMY-2 levels at the cortex increased from anaphase onset for about a minute, peaking at the time of furrow initiation, after which they gradually decreased (Figure 2E). HMR-1 depletion led to a significant increase in the level of cortical NMY-2 throughout the measured period (Figures 2D and 2E). We did not detect a significant change in the global amount of NMY-2 or levels of cortical F-actin in *hmr-1(RNAi)* embryos compared with unperturbed controls (Figures S2A and S2B), suggesting that the increase in cortical levels of NMY-2 was due to increased recruitment of NMY-2 upon HMR-1 depletion. In contrast to the contact-free cell surface, the intensity of NMY-2 at the ingression furrow showed no difference between control and *hmr-1(RNAi)* embryos (Figure 2F). This result is in agreement with the fact that the cytokinetic furrow was devoid of HMR-1 to begin with; therefore, loss of HMR-1 would have little effect on the levels of NMY-2 in the furrow. To check whether increased NMY-2 levels upon HMR-1 depletion were due to altered turnover of cortical NMY-2, we measured fluorescence recovery after photobleaching in the anterior cortex of maintenance-phase embryos expressing NMY-2::GFP. Control and *hmr-1(RNAi)* embryos displayed similar NMY-2::GFP recovery kinetics after bleach (Figure S2C), suggesting no significant difference in molecular turnover rate of NMY-2::GFP.

PAR proteins and HMR-1 have been known to reciprocally regulate the functioning of each other in *C. elegans* embryos [9, 19–21]. Therefore, we checked whether the effect of HMR-1 on cortical NMY-2 was due to polarity deregulation by imaging embryos co-expressing GFP::PAR2 and mCherry::PAR6 in control and *hmr-1(RNAi)* embryos. Loss of HMR-1 had no detectable influence on PAR protein localization in one-cell, two-cell, or

four-cell stages (Figure S2D), suggesting that the increase in cortical NMY-2 in *hmr-1(RNAi)* embryos was PAR independent.

The antagonism we describe between HMR-1 and NMY-2 in *C. elegans* embryos is strikingly different from cultured mammalian epithelial sheets, in which E-cadherin reportedly recruits and co-localizes with myosin II [5, 22, 23]. However, our findings are consistent with studies in *Drosophila* and the early mouse embryo, wherein E-cadherin was found to negatively regulate the localization of myosin II [24, 25].

Non-junctional HMR-1 Downregulates RHO-1 Activity and CYK-1 Localization at the Cortex

RHO-1 GTPase activity has been shown in various models to be required for recruitment and activation of myosin II contractility at the cortex [26]. We therefore tested for any change in cortical RHO-1 activity upon HMR-1 depletion and detected a significant increase in cortical RHO-1 activity in *hmr-1(RNAi)* embryos (Figure 2G), as measured by the accumulation of the RHO-1-binding domain of *anillin* fused to GFP [27]. Furthermore, we also measured an increase in the amount of the formin CYK-1 at the cortex upon HMR-1 depletion (Figure 2H). CYK-1 is an ortholog of *Drosophila* diaphanous, which is a downstream target of RhoA and is known to polymerize F-actin, that can associate with myosin II [26, 28]. Thus, it appears very likely that non-junctional HMR-1 clusters modulate cortical NMY-2 by regulating RHO-1 and CYK-1 activity at the cell surface.

Regulation of Rho GTPases by E-cadherin at cell-cell junctions was previously reported [29, 30]. Our results extend these observations by showing that non-junctional E-cadherin can also regulate Rho GTPases. This is consistent with the observation that non-adhesive E-cadherin was found to interact with many of the same proteins as junctional cadherin [31].

HMR-1 Clusters Slow Down Cytokinetic Furrow Ingression

An important function of the actomyosin cortex in eukaryotic cells is to drive cell division [32–34]. Given the inhibitory effect of non-junctional HMR-1 clusters on NMY-2 localization, we tested whether the expression level of HMR-1 has an effect on the initiation and ingression rate of the cytokinetic furrow during the first cell division. Anaphase onset was determined by following nuclear dynamics with mCherry-tagged histone, whereas the furrow was tracked using the membrane marker mCherry::PLC1 δ -PH. In both control and *hmr-1(RNAi)* embryos, the first sign of a furrow in the membrane was detected ~ 70 s after anaphase onset. From that point on, the time it took control embryos to complete furrow ingression was 166 ± 8 s. In contrast, *hmr-1(RNAi)* embryos completed furrow ingression in 144 ± 8 s, corresponding to a 13% decrease in furrowing time (Figures 3A–3C). Conversely, doubling the amount of HMR-1

(D) Pearson's coefficient of correlation (PCC) calculated between HMR-1::GFP and Lifeact::RFP from all of the line scans plotted in (C, ii). Error bars are mean \pm 95% confidence interval [CI].

(E) Time series of the ROI in the anterior cortex showing a cortical F-actin filament (arrowheads) sweeping the HMR-1::GFP cluster (arrows) along during cortical flow. F-actin trails the HMR-1 cluster in frame 1; in frame 7, they are seen to be co-localizing; whereas in frame 12, F-actin surges ahead, dragging and stretching the HMR-1 cluster along.

(F) Scatterplot showing the mean $|V_Y|_{\max}$ of HMR-1 clusters and F-actin at the anterior cortex during cytokinesis-associated cortical rotation estimated using PIV ($n = 14$ embryos).

Error bars denote 95% CI (** $p < 0.005$, *** $p < 0.0001$, Mann-Whitney U test). Error bars are mean \pm 95% CI. See also Figure S1 and Movies S1 and S2.

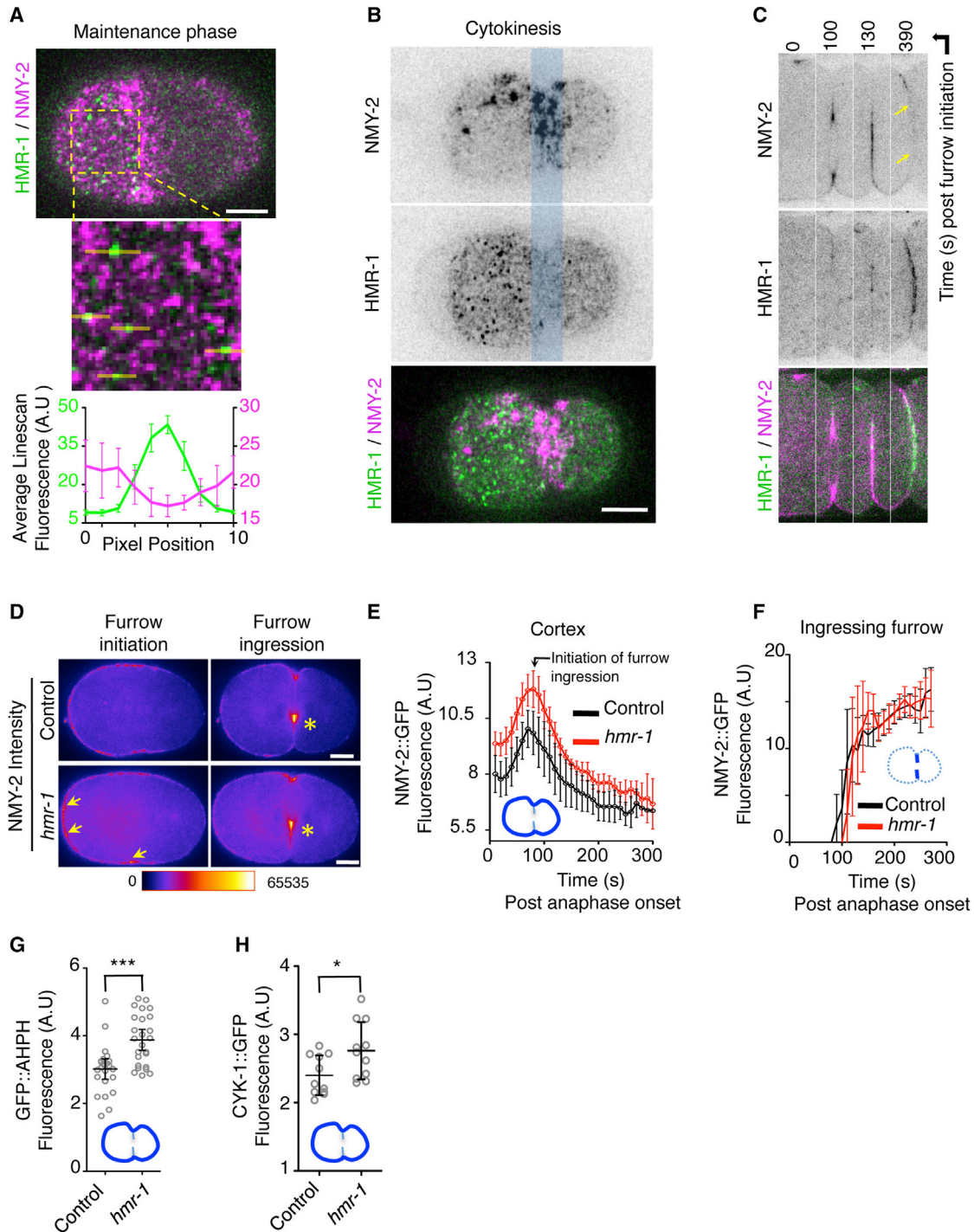


Figure 2. HMR-1 Clusters Negatively Regulate NMY-2 and RHO-1 Activity at the Cortex

(A) HMR-1::GFP and NMY-2::mCherry display mutual exclusion at the anterior cortex. Line scans are denoted as yellow lines in the enlarged ROI. Average two-color intensity profile plot ($n = 8$ embryos, $n = 30$ line scans) showing spatial segregation of HMR-1::GFP and NMY-2::mCherry. Error bars are mean \pm SEM. (B) Surface view of an embryo co-expressing HMR-1::GFP and NMY-2::mCherry undergoing cytokinesis. The furrow region (gray shade) is enriched in NMY-2::mCherry but mostly devoid of HMR-1::GFP puncta.

(C) Time-lapse images of furrow ingression during the first division in an embryo co-expressing HMR-1::GFP and NMY-2::mCherry depicting their distinct temporal localization during and after cytokinesis. Arrows indicate diminishing NMY-1::mCherry at the newly formed cell-cell interface after cytokinesis.

(D) Equatorial plane showing NMY-2::GFP levels (pseudo-colored) at the cortex (arrows) and ingressing furrow (asterisks) in control and *hmr-1(RNAi)* embryos. (E) Mean and 95% CI of NMY-2::GFP intensity measured along the contact-free surface in control (black curve) and *hmr-1(RNAi)* (red curve) embryos ($n = 11$) from anaphase onset ($t = 0$ s) until completion of furrow ingression. Inset: the ROI measured is indicated in dark blue in the cartoon.

(legend continued on next page)

by expressing HMR-1::GFP under the *mex-5* promoter on top of endogenous HMR-1 (Figures S3A and S3B) delayed the completion of furrow ingression by 13% and resulted in furrow ingression taking 187 ± 10 s (Figures 3A–3C). Depletion of HMR-1 did not affect the size of embryos, as control and *hmr-1(RNAi)* embryos had similar widths, measuring ~ 36 μm at anaphase onset (Figure S3C). Thus, surface-localized HMR-1 clusters negatively regulated the furrow closure speed in a dose-dependent mechanism (Figure 3D). We also measured the time taken for furrow ingression of the second and third cell divisions and, similar to the first division, found them to be significantly shorter in *hmr-1(RNAi)* embryos compared to controls (Figures S3D and S3E). The cytokinetic furrow during AB division was assembled along the AB-P1 cell boundary in 15/15 control embryos. However, *hmr-1(RNAi)* embryos undergoing AB cell division displayed aberrant furrow positioning (6/12 embryos) and, in embryos that managed to assemble the cytokinetic furrow along the AB-P1 boundary, subsequent constriction resulted in cortical deformation and inter-cellular spaces (Figure S3F, inset). Loss of HMR-1 also resulted in a reduced interface angle between AB and P1 cells, most likely due to loss of adhesion and/or increased cortical contractility (Figure S3G). Whereas HMR-1 regulates furrow ingression kinetics independent of adhesion in the one-cell-stage division, during the subsequent embryonic cell divisions HMR-1-mediated adhesive forces could also contribute to regulating cytokinetic furrow ingression, akin to the “tug-of-war” model proposed from studies in *Drosophila* epithelial tissues [35, 36].

HMR-1 Regulates Cytokinesis via Its Cytoplasmic Domain

Our observation that cytokinetic furrow ingression is slowed down by HMR-1 in a dose-dependent manner in a one-cell-stage embryo suggested an adhesion-independent mechanism for regulation of the actomyosin cortex by HMR-1. However, the extra-cellular domain of HMR-1 assembled into the non-junctional clusters could, in theory, still interact with the permeability barrier surrounding the plasma membrane of the zygote [37], thereby providing resistance to cortical deformation. To rule out this possibility, we expressed a membrane-tethered HMR-1 intra-cellular domain (ICD) or an ICD missing the catenin-binding region (ICD^M) from a heat shock promoter [9] in the germline (Figure S3H) and imaged the effect of expressed transgenes on cytokinesis in the zygote. mCherry-tagged histone was used to mark anaphase onset, and cortical ingression during cytokinesis was detected by Lifeact::RFP. Heat-shocked embryos expressing HMR-1 ICD took 222 ± 25 s to complete furrow ingression, which was significantly longer than the time for heat-shocked control embryos (191 ± 27 s) or un-induced embryos carrying the *ha::PLC1 δ -PH::hmr-1^{ICD}* transgene (190 ± 22 s)

(Figures 3E and 3F), demonstrating that slowing down of furrow ingression was specifically mediated by HMR-1 ICD and not its extra-cellular domain. In contrast, expression of HMR-1 ICD^M did not affect cytokinesis (174 ± 29 s) compared to un-induced embryos (179 ± 32 s), suggesting that an interaction with catenins is essential for the slowing of cytokinesis. Therefore, we tested whether depletion of JAC-1, the p120 catenin ortholog [38], or HMP-2, the beta-catenin ortholog [7], would affect cytokinetic furrowing speed. We found that RNAi of JAC-1 had no effect on the time taken for furrow ingression in the zygote; however, depletion of HMP-2 led to a significant shortening of the time taken for the first cytokinesis (Figure 3G). Thus, HMP-2 most likely mediates the interaction of HMR-1 with F-actin, although the precise nature of this interaction remains to be elucidated.

HMR-1 Clusters Regulate Cytokinesis Independent of Their Effect on Cortical NMY-2 Levels

Because HMR-1 depletion increased NMY-2 levels at the cortex, we asked whether the augmentation of NMY-2 was responsible for the increase in furrow ingression rate. For this, we looked for circumstances under which HMR-1 depletion would not increase the level of NMY-2. The *C. elegans* ortholog of Rho kinase, LET-502, activates NMY-2 contractility during cytokinesis [39]. Accordingly, NMY-2 failed to accumulate at the cortex after anaphase onset in *let-502;sas-5(RNAi)* embryos (Figure 4A). Cortical NMY-2 levels remained unchanged even when HMR-1 was depleted in *let-502(RNAi)* embryos. Levels of NMY-2 localized to the ingressing furrow were also similar between *let-502;sas-5(RNAi)* and *let-502;hmr-1(RNAi)* (Figure S4A). *sas-5* was used as a control to account for the dilution of the RNAi machinery due to the combination of two dsRNAs [40]. We therefore compared the furrow ingression in *let-502;sas-5(RNAi)* and *let-502;hmr-1(RNAi)* embryos, and found that the time taken for furrow ingression after anaphase onset decreased by $\sim 19\%$ in *let-502;hmr-1(RNAi)* (334 ± 38 s) when compared to *let-502;sas-5(RNAi)* (412 ± 26 s) (Figures 4B and 4C). These results show that non-junctional HMR-1 can regulate cytokinetic furrowing speeds irrespective of cortical NMY-2 levels, suggesting an NMY-2-independent mechanism through which non-junctional HMR-1 clusters slow down cytokinesis.

HMR-1 Clusters Provide Drag during Cortical Flows

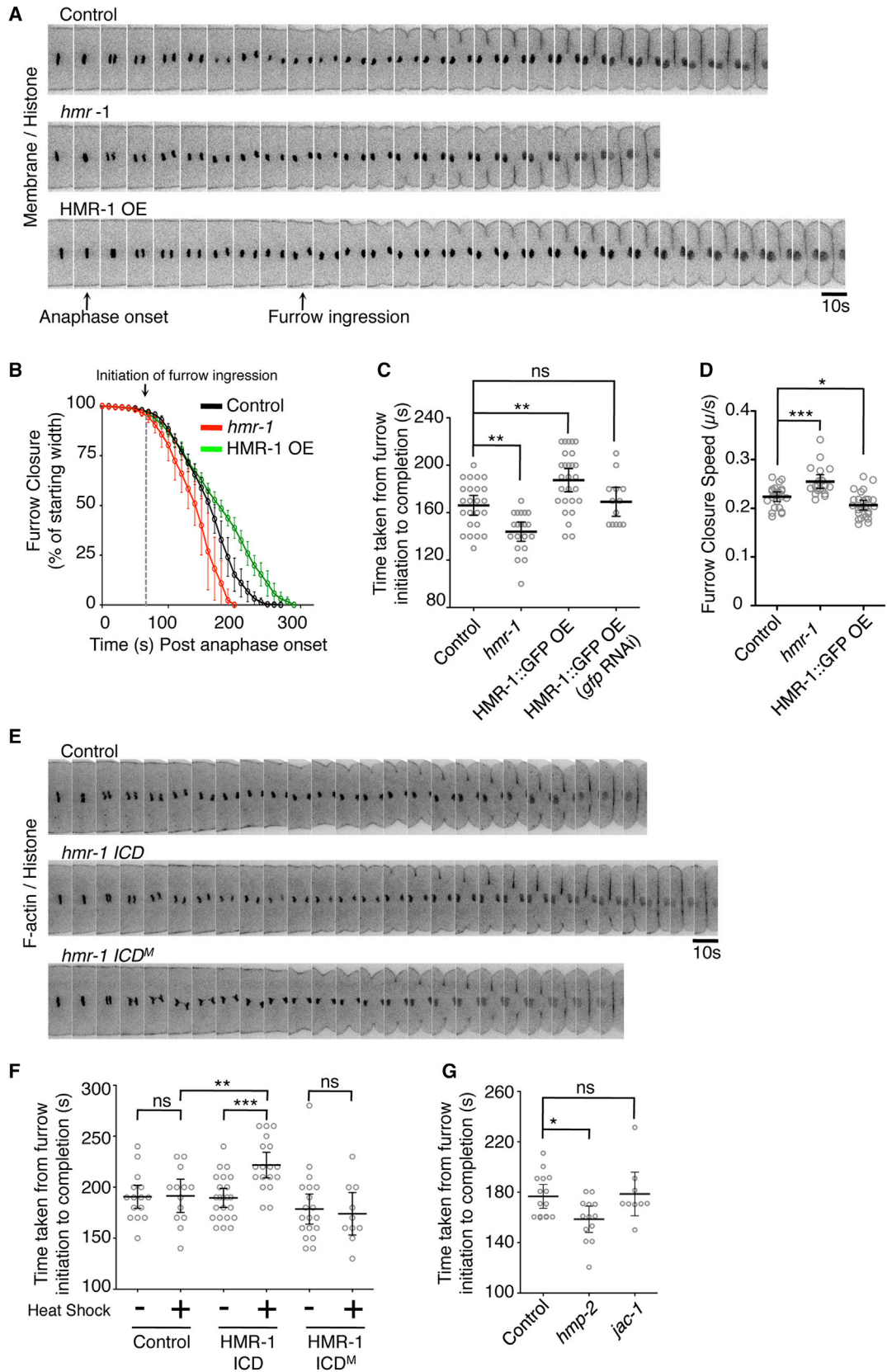
Given our observation that cortical F-actin moves faster than HMR-1 and appears to drag HMR-1 clusters that are anchored in the plasma membrane (Figures 1F and 1G), we hypothesized that HMR-1 might slow cortical movement by adding structural impediments. Consistent with this idea, when we analyzed cortical F-actin dynamics in embryos lacking or overexpressing HMR-1 using PIV, we found the mean $|V_Y|_{\text{max}}$ of F-actin during cytokinesis-associated cortical rotation in *hmr-1(RNAi)* embryos

(F) Mean and 95% CI of NMY-2::GFP intensity measured along the ingressing furrow in control (black curve) and *hmr-1(RNAi)* (red curve) embryos ($n = 11$) from anaphase onset ($t = 0$ s) until completion of furrow ingression. Inset: the ROI measured is indicated in dark blue in the cartoon.

(G) Scatterplot showing mean and 95% CI of GFP::AHPH intensity (“RHO-1 activity sensor”) measured along the cortical surface in control and *hmr-1(RNAi)* embryos at the start of furrow ingression (** $p < 0.0001$, Mann-Whitney U test).

(H) Scatterplot showing mean and 95% CI of (endogenous) CYK-1::GFP intensity measured along the cortical surface in control and *hmr-1(RNAi)* embryos at the start of furrow invagination (* $p < 0.05$, Mann-Whitney U test).

See also Figure S2.



(legend on next page)

($0.48 \pm 0.05 \mu\text{m/s}$; $N = 30$) was significantly faster than the mean $|V_Y|_{\text{max}}$ in embryos overexpressing HMR-1 ($0.44 \pm 0.07 \mu\text{m/s}$; $N = 27$) (Figure 4D). The corresponding mean $|V_X|_{\text{max}}$ was also faster in *hmr-1(RNAi)* embryos ($0.13 \pm 0.04 \mu\text{m/s}$; $N = 30$) compared to HMR-1-overexpressing embryos ($0.11 \pm 0.03 \mu\text{m/s}$; $N = 30$), suggesting that loss of HMR-1 clusters led to increased mobility of cortical actomyosin. To further test this idea, we manually tracked and measured the cortical flow velocity of NMY-2 puncta in two regions of the zygote: the future furrow region, which did not contain HMR-1 clusters, and a more anterior region that did (Figure 4E; Movie S3). In all embryos examined ($N = 16$), we found $|V_Y|_{\text{max}}$ of NMY-2 foci to be significantly higher in the furrow region devoid of HMR-1 clusters. Moreover, in embryos depleted of HMR-1 ($N = 12$), there was no difference in flow velocity between anterior and future furrow regions (Figure 4E). Put together, our results suggest that the slower cortical flow in the anterior was indeed due to drag imparted by HMR-1 clusters.

These results are in agreement with the “picket fence” model proposed by Sako et al. [6], except that in their system, E-cadherin movement was hindered by the F-actin “fences” whereas here it is E-cadherin that impedes the movement of F-actin.

HMR-1 Clusters Help Maintain the Integrity of the Actomyosin Cortex

Because HMR-1 spans the plasma membrane and interacts with the underlying cortex, we then investigated whether HMR-1 stabilized the actomyosin cortex at the embryonic cell surface. We observed a temporary splitting of the NMY-2 signal at the anterior cortex of the embryo during the initial stages of cytokinetic furrow ingression. Simultaneous imaging of the plasma membrane showed that whereas some NMY-2 remained co-localized with the membrane, a segment of the cortex detached and moved inward (Figure 4F). Such splitting of the cortex was more extensive and lasted significantly longer in the *hmr-1(RNAi)* embryos (46 ± 7 s) compared with control embryos (15 ± 7 s) (Figures 4G and 4H; Movie S4). The cortical tear in *hmr-1(RNAi)* embryos could be explained by a contribution of HMR-1 clusters to the stabilization of the cortex adjacent to the plasma membrane and/or by the increase in NMY-2 levels at the cortex, resulting in greater contractile forces. Increasing NMY-2 activity alone, by depleting the myosin light chain phosphatase *mel-11*, did not lead to increased cortical splitting. Conversely, reducing NMY-2 activity, by depleting the Rho kinase *let-502*,

rescued the cortical detachment phenotype in *hmr-1(RNAi)* embryos (Figure 4H), suggesting that both an increase in cortical contractility and a loss of stabilizing linkages are responsible for the cortical detachment phenotype in *hmr-1(RNAi)* embryos. In the majority of *hmr-1(RNAi)* embryos, the gap between the split cortex eventually closed. However, in 10% of embryos depleted of HMR-1 ($N = 40$), the cortex split and the inner segment remained dissociated from the cortical fragment that was attached and supported the plasma membrane for the duration of several rounds of cell division (Figure 4I).

In conclusion, our observations in the *C. elegans* zygote extend the role of E-cadherin/HMR-1 beyond the cell-cell junctions to the entire cortex. We propose that non-junctional HMR-1 clusters influence cellular cortical dynamics, such as actomyosin flow and cytokinesis, by (1) providing mechanical resistance to cortical deformations and (2) decreasing RHO-1 activity and NMY-2 levels at the cortex, although the latter is not strictly required for the effect of HMR-1 on cytokinesis kinetics. Thus, our work uncovered a non-canonical role for E-cadherin clusters that is adhesion independent and yet important for the regulation of cell-shape dynamics. Therefore, future work on cadherin’s role in physiology and disease must also take into account the cortical functions of non-junctional cadherin clusters.

EXPERIMENTAL PROCEDURES

Detailed experimental procedures are provided in the [Supplemental Experimental Procedures](#).

SUPPLEMENTAL INFORMATION

Supplemental Information includes Supplemental Experimental Procedures, four figures, and four movies and can be found with this article online at <http://dx.doi.org/10.1016/j.cub.2016.10.032>.

AUTHOR CONTRIBUTIONS

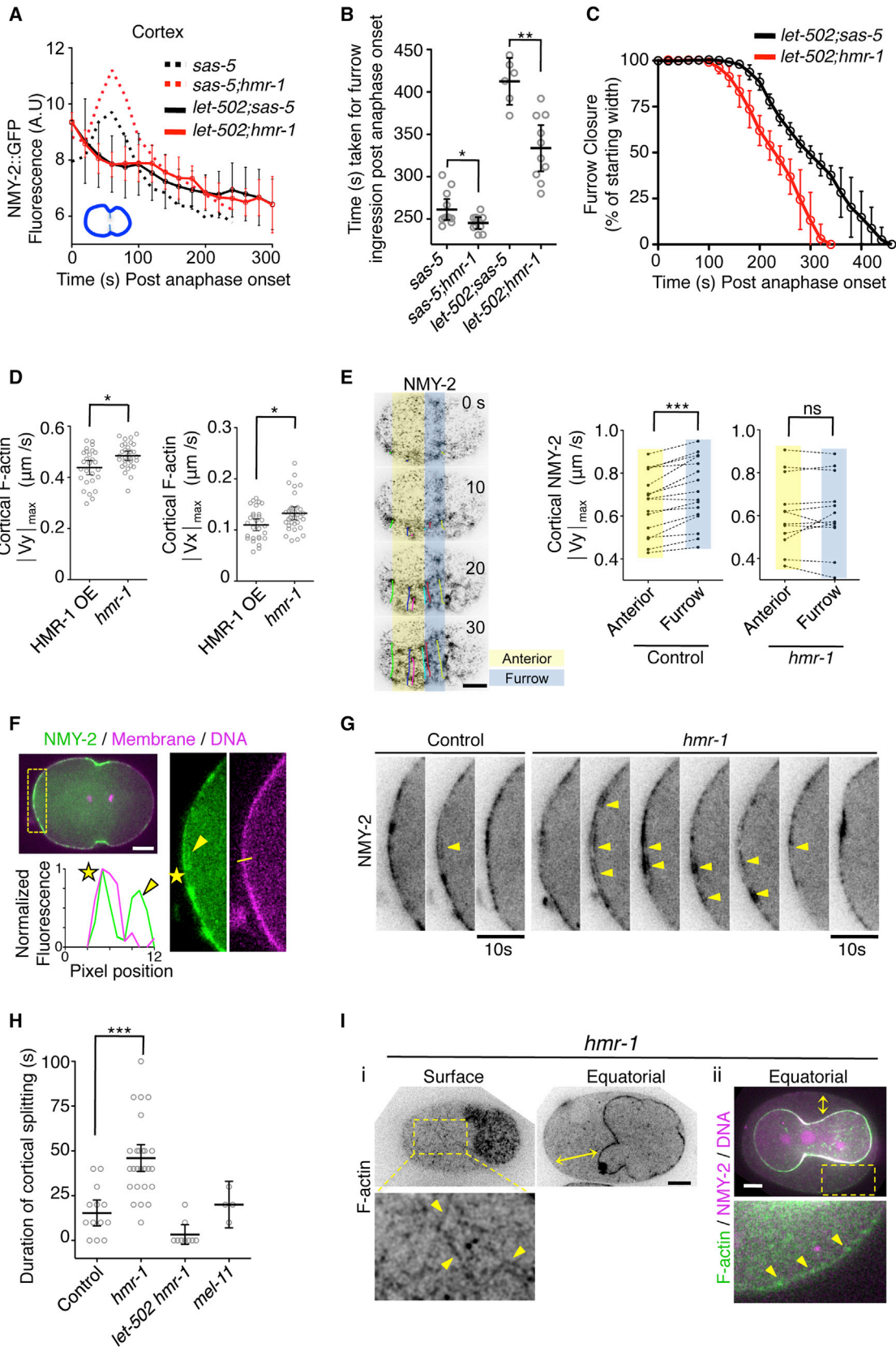
A.P. and R.Z.-B. conceived the project. A.P. designed and performed the experiments. H.T.O. contributed analytic tools. A.P. and R.Z.-B. analyzed the data and wrote the manuscript.

ACKNOWLEDGMENTS

This work was supported by the National Research Foundation Singapore under its NRF fellowship (NRF-RF2009-RF001-074, awarded to R.Z.-B.) and a CRP grant CRP001-084, and by a Ministry of Education Tier 2 grant (MOE2015-T2-1-045). We thank Jeremy Nance, Karen Oegema, Michael

Figure 3. HMR-1 Slows Down Cytokinetic Furrow Ingression Independent of Its Extra-cellular Domain

- (A) Time-lapse confocal images of an equatorial plane showing ingression of the first cytokinetic furrow in control, *hmr-1(RNAi)*, and HMR-1::GFP-overexpressing (OE) embryos co-expressing mCherry::PLC1 δ -PH and Histone::mCherry.
- (B) Kinetics of cytokinetic furrow closure after anaphase onset as measured by the percentage of furrow ingression in control ($n = 24$), *hmr-1(RNAi)* ($n = 20$), and HMR-1::GFP OE ($n = 27$) embryos. Initiation of furrow ingression is marked as the time at which cell-membrane indentation is observed.
- (C) Quantification of the time taken from furrow initiation to furrow closure in control, *hmr-1(RNAi)*, HMR-1::GFP OE, and HMR-1::GFP; *gfp(RNAi)* ($n = 13$).
- (D) Plot showing mean furrow closure speeds for the embryos analyzed in (B) calculated from the time of initiation of furrow ingression.
- (E) Time-lapse confocal images of an equatorial plane showing ingression of the first cytokinetic furrow in heat-shock-induced control (no transgene) and HMR-1 ICD- and HMR-1 ICD^M-expressing embryos co-expressing Lifeact::RFP and Histone::mCherry.
- (F) Quantification of the time taken from furrow initiation to furrow closure in un-induced and induced embryos from control ($n = 23$) and *hmr-1 ICD* ($n = 18$)- and *hmr-1 ICD^M* ($n = 10$)-carrying worms.
- (G) Scatterplot showing the quantification of the time taken from furrow initiation to furrow closure in control, *hmp-2*, and *jac-1 RNAi* embryos expressing GFP::PLC1 δ -PH and Histone::mCherry.
- Error bars are mean \pm 95% CI (* $p < 0.05$, ** $p < 0.005$, *** $p < 0.0001$, Mann-Whitney U test). See also [Figure S3](#).



(legend on next page)

Glotzer, Zhirong Bao, Fumio Motegi, and Tricia Low for sharing strains and Jeff Hardin for the anti-HMR-1 antibody. Some strains were provided by the CGC, which is funded by the NIH Office of Research Infrastructure Programs (P40 OD010440). We thank Fumio Motegi for discussions.

Received: April 10, 2016

Revised: September 16, 2016

Accepted: October 19, 2016

Published: December 15, 2016

REFERENCES

- Harris, T.J., and Tepass, U. (2010). Adherens junctions: from molecules to morphogenesis. *Nat. Rev. Mol. Cell Biol.* *11*, 502–514.
- Takeichi, M. (2014). Dynamic contacts: rearranging adherens junctions to drive epithelial remodelling. *Nat. Rev. Mol. Cell Biol.* *15*, 397–410.
- Zaidel-Bar, R. (2013). Cadherin adhesome at a glance. *J. Cell Sci.* *126*, 373–378.
- Wu, Y., Kanchanawong, P., and Zaidel-Bar, R. (2015). Actin-delimited adhesion-independent clustering of E-cadherin forms the nanoscale building blocks of adherens junctions. *Dev. Cell* *32*, 139–154.
- Borghini, N., Sorokina, M., Shcherbakova, O.G., Weis, W.I., Pruitt, B.L., Nelson, W.J., and Dunn, A.R. (2012). E-cadherin is under constitutive actomyosin-generated tension that is increased at cell-cell contacts upon externally applied stretch. *Proc. Natl. Acad. Sci. USA* *109*, 12568–12573.
- Sako, Y., Nagafuchi, A., Tsukita, S., Takeichi, M., and Kusumi, A. (1998). Cytoplasmic regulation of the movement of E-cadherin on the free cell surface as studied by optical tweezers and single particle tracking: corralling and tethering by the membrane skeleton. *J. Cell Biol.* *140*, 1227–1240.
- Costa, M., Raich, W., Agbunag, C., Leung, B., Hardin, J., and Priess, J.R. (1998). A putative catenin-cadherin system mediates morphogenesis of the *Caenorhabditis elegans* embryo. *J. Cell Biol.* *141*, 297–308.
- Nance, J., and Priess, J.R. (2002). Cell polarity and gastrulation in *C. elegans*. *Development* *129*, 387–397.
- Klompstra, D., Anderson, D.C., Yeh, J.Y., Zilberman, Y., and Nance, J. (2015). An instructive role for *C. elegans* E-cadherin in translating cell contact cues into cortical polarity. *Nat. Cell Biol.* *17*, 726–735.
- Chihara, D., and Nance, J. (2012). An E-cadherin-mediated hitchhiking mechanism for *C. elegans* germ cell internalization during gastrulation. *Development* *139*, 2547–2556.
- Grana, T.M., Cox, E.A., Lynch, A.M., and Hardin, J. (2010). SAX-7/L1CAM and HMR-1/cadherin function redundantly in blastomere compaction and non-muscle myosin accumulation during *Caenorhabditis elegans* gastrulation. *Dev. Biol.* *344*, 731–744.
- Schonegg, S., Hyman, A.A., and Wood, W.B. (2014). Timing and mechanism of the initial cue establishing handed left–right asymmetry in *Caenorhabditis elegans* embryos. *Genesis* *52*, 572–580.
- Liu, J., Maduzia, L.L., Shirayama, M., and Mello, C.C. (2010). NMY-2 maintains cellular asymmetry and cell boundaries, and promotes a SRC-dependent asymmetric cell division. *Dev. Biol.* *339*, 366–373.
- Munro, E., Nance, J., and Priess, J.R. (2004). Cortical flows powered by asymmetrical contraction transport PAR proteins to establish and maintain anterior-posterior polarity in the early *C. elegans* embryo. *Dev. Cell* *7*, 413–424.
- Han, S.P., and Yap, A.S. (2012). The cytoskeleton and classical cadherin adhesions. *Subcell. Biochem.* *60*, 111–135.
- Strome, S. (1986). Fluorescence visualization of the distribution of microfilaments in gonads and early embryos of the nematode *Caenorhabditis elegans*. *J. Cell Biol.* *103*, 2241–2252.
- Naganathan, S.R., Fürthauer, S., Nishikawa, M., Jülicher, F., and Grill, S.W. (2014). Active torque generation by the actomyosin cell cortex drives left-right symmetry breaking. *eLife* *3*, e04165.
- Mayer, M., Depken, M., Bois, J.S., Jülicher, F., and Grill, S.W. (2010). Anisotropies in cortical tension reveal the physical basis of polarizing cortical flows. *Nature* *467*, 617–621.
- Cheeks, R.J., Canman, J.C., Gabriel, W.N., Meyer, N., Strome, S., and Goldstein, B. (2004). *C. elegans* PAR proteins function by mobilizing and stabilizing asymmetrically localized protein complexes. *Curr. Biol.* *14*, 851–862.
- Achilleos, A., Wehman, A.M., and Nance, J. (2010). PAR-3 mediates the initial clustering and apical localization of junction and polarity proteins during *C. elegans* intestinal epithelial cell polarization. *Development* *137*, 1833–1842.
- Totong, R., Achilleos, A., and Nance, J. (2007). PAR-6 is required for junction formation but not apicobasal polarization in *C. elegans* embryonic epithelial cells. *Development* *134*, 1259–1268.
- Shewan, A.M., Maddugoda, M., Kraemer, A., Stehens, S.J., Verma, S., Kovacs, E.M., and Yap, A.S. (2005). Myosin 2 is a key Rho kinase target necessary for the local concentration of E-cadherin at cell-cell contacts. *Mol. Biol. Cell* *16*, 4531–4542.
- Smutny, M., Cox, H.L., Leerberg, J.M., Kovacs, E.M., Conti, M.A., Ferguson, C., Hamilton, N.A., Parton, R.G., Adelstein, R.S., and Yap, A.S. (2010). Myosin II isoforms identify distinct functional modules that support integrity of the epithelial zonula adherens. *Nat. Cell Biol.* *12*, 696–702.
- Maître, J.L., Niwayama, R., Turlier, H., Nédélec, F., and Hiragi, T. (2015). Pulsatile cell-autonomous contractility drives compaction in the mouse embryo. *Nat. Cell Biol.* *17*, 849–855.

Figure 4. HMR-1 Dampens Cortical Flow and Reinforces Cortical Integrity Independent of Its NMY-2 Regulation

(A) Mean cortical NMY-2::GFP intensity in *sas-5(RNAi)* (dotted black curve), *sas-5;hmr-1(RNAi)* (dotted red curve), *let-502;sas-5(RNAi)* (solid black curve), and *let-502;hmr-1(RNAi)* (solid red curve) embryos measured from anaphase onset. Inset: blue cartoon indicates the measured ROI.

(B) Time taken for furrow ingression in *sas-5(RNAi)*, *sas-5;hmr-1(RNAi)*, *let-502;sas-5(RNAi)*, and *let-502;hmr-1(RNAi)* embryos analyzed in (A) ($n > 8$ embryos; ** $p < 0.005$, Mann-Whitney U test).

(C) Kinetics of cytokinetic furrow closure after anaphase onset as measured by the percentage of furrow ingression in *let-502;sas-5(RNAi)* (black curve) and *let-502;hmr-1(RNAi)* (red curve) embryos. See also [Figure S4](#).

(D) Scatterplot showing the mean $|V_{y}|_{\max}$ (left) and $|V_{x}|_{\max}$ (right) estimated from PIV analysis of F-actin at the anterior cortex in HMR-1 OE ($n = 29$ embryos) and *hmr-1(RNAi)* ($n = 29$ embryos) during cytokinesis-associated cortical rotation (** $p < 0.005$, Mann-Whitney U test).

(E) Movement of individual NMY-2::GFP foci (colored tracks) in the region of the future furrow (gray shade) and the anterior cortex (yellow shade) was used to quantify flow rates. Scatterplot of $|V_{y}|_{\max}$ estimated from manually tracking the NMY-2 foci in the anterior cortex and the region of the future furrow in control ($n = 15$) and *hmr-1(RNAi)* ($n = 12$) embryos. Each point is the average of >5 foci measured, and each pair of points represents a separate embryo (** $p < 0.001$, Wilcoxon matched-pairs signed-rank test). See also [Movie S3](#).

(F) A small and temporary splitting of the cortex (NMY-2::GFP) is observed in a control embryo at the onset of furrow ingression. Although one part of the cortical layer remains attached to the membrane (star), the split results in another part moving slightly into the cytoplasm (arrowhead).

(G) Splitting of the cortex is more extensive (arrowheads) and lasts longer in an *hmr-1(RNAi)* embryo.

(H) Quantification of the duration of cortex splitting in indicated embryos (** $p < 0.0001$, Mann-Whitney U test).

(I) Less common extreme phenotype of *hmr-1(RNAi)* embryos, in which the cortex splits into two parts, with one completely detached from the cell surface (a “cell within a cell”) and the other part remaining attached to the membrane (arrowheads). Error bars denote 95% CI. See also [Movie S4](#).

25. Levayer, R., Pelissier-Monier, A., and Lecuit, T. (2011). Spatial regulation of Dia and Myosin-II by RhoGEF2 controls initiation of E-cadherin endocytosis during epithelial morphogenesis. *Nat. Cell Biol.* **13**, 529–540.
26. Jaffe, A.B., and Hall, A. (2005). Rho GTPases: biochemistry and biology. *Annu. Rev. Cell Dev. Biol.* **21**, 247–269.
27. Tse, Y.C., Werner, M., Longhini, K.M., Labbe, J.C., Goldstein, B., and Glotzer, M. (2012). RhoA activation during polarization and cytokinesis of the early *Caenorhabditis elegans* embryo is differentially dependent on NOP-1 and CYK-4. *Mol. Biol. Cell* **23**, 4020–4031.
28. Severson, A.F., Baillie, D.L., and Bowerman, B. (2002). A formin homology protein and a profilin are required for cytokinesis and Arp2/3-independent assembly of cortical microfilaments in *C. elegans*. *Curr. Biol.* **12**, 2066–2075.
29. Noren, N.K., Niessen, C.M., Gumbiner, B.M., and Burridge, K. (2001). Cadherin engagement regulates Rho family GTPases. *J. Biol. Chem.* **276**, 33305–33308.
30. Ratheesh, A., Gomez, G.A., Priya, R., Verma, S., Kovacs, E.M., Jiang, K., Brown, N.H., Akhmanova, A., Stehbens, S.J., and Yap, A.S. (2012). Centralspindlin and α -catenin regulate Rho signalling at the epithelial zonula adherens. *Nat. Cell Biol.* **14**, 818–828.
31. Guo, Z., Neilson, L.J., Zhong, H., Murray, P.S., Zanivan, S., and Zaidel-Bar, R. (2014). E-cadherin interactome complexity and robustness resolved by quantitative proteomics. *Sci. Signal.* **7**, rs7.
32. Robinson, D.N., and Spudich, J.A. (2004). Mechanics and regulation of cytokinesis. *Curr. Opin. Cell Biol.* **16**, 182–188.
33. Clark, A.G., Wartlick, O., Salbreux, G., and Paluch, E.K. (2014). Stresses at the cell surface during animal cell morphogenesis. *Curr. Biol.* **24**, R484–R494.
34. Werner, M., and Glotzer, M. (2008). Control of cortical contractility during cytokinesis. *Biochem. Soc. Trans.* **36**, 371–377.
35. Guillot, C., and Lecuit, T. (2013). Adhesion disengagement uncouples intrinsic and extrinsic forces to drive cytokinesis in epithelial tissues. *Dev. Cell* **24**, 227–241.
36. Herszterg, S., Leibfried, A., Bosveld, F., Martin, C., and Bellaiche, Y. (2013). Interplay between the dividing cell and its neighbors regulates adherens junction formation during cytokinesis in epithelial tissue. *Dev. Cell* **24**, 256–270.
37. Olson, S.K., Greenan, G., Desai, A., Müller-Reichert, T., and Oegema, K. (2012). Hierarchical assembly of the eggshell and permeability barrier in *C. elegans*. *J. Cell Biol.* **198**, 731–748.
38. Pettitt, J., Cox, E.A., Broadbent, I.D., Flett, A., and Hardin, J. (2003). The *Caenorhabditis elegans* p120 catenin homologue, JAC-1, modulates cadherin-catenin function during epidermal morphogenesis. *J. Cell Biol.* **162**, 15–22.
39. Piekny, A.J., and Mains, P.E. (2002). Rho-binding kinase (LET-502) and myosin phosphatase (MEL-11) regulate cytokinesis in the early *Caenorhabditis elegans* embryo. *J. Cell Sci.* **115**, 2271–2282.
40. Maddox, A.S., Lewellyn, L., Desai, A., and Oegema, K. (2007). Anillin and the septins promote asymmetric ingression of the cytokinetic furrow. *Dev. Cell* **12**, 827–835.

Current Biology, Volume 27

Supplemental Information

**Non-junctional E-Cadherin Clusters Regulate
the Actomyosin Cortex in the *C. elegans* Zygote**

Anup Padmanabhan, Hui Ting Ong, and Ronen Zaidel-Bar

Figure S1

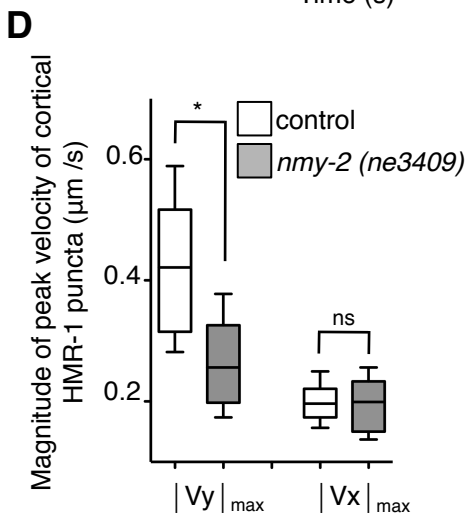
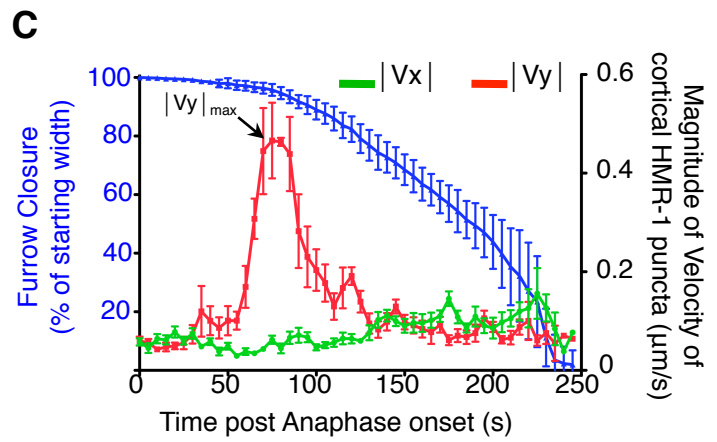
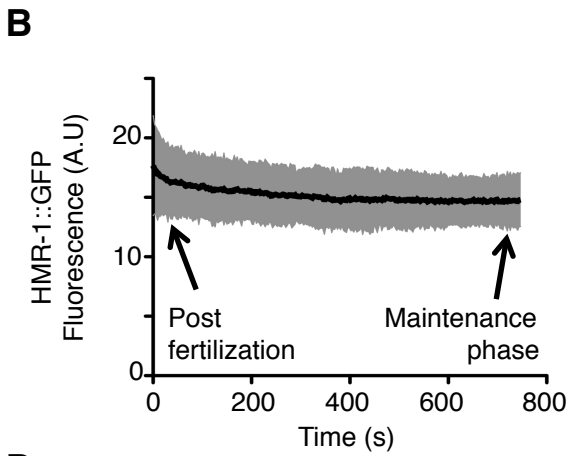
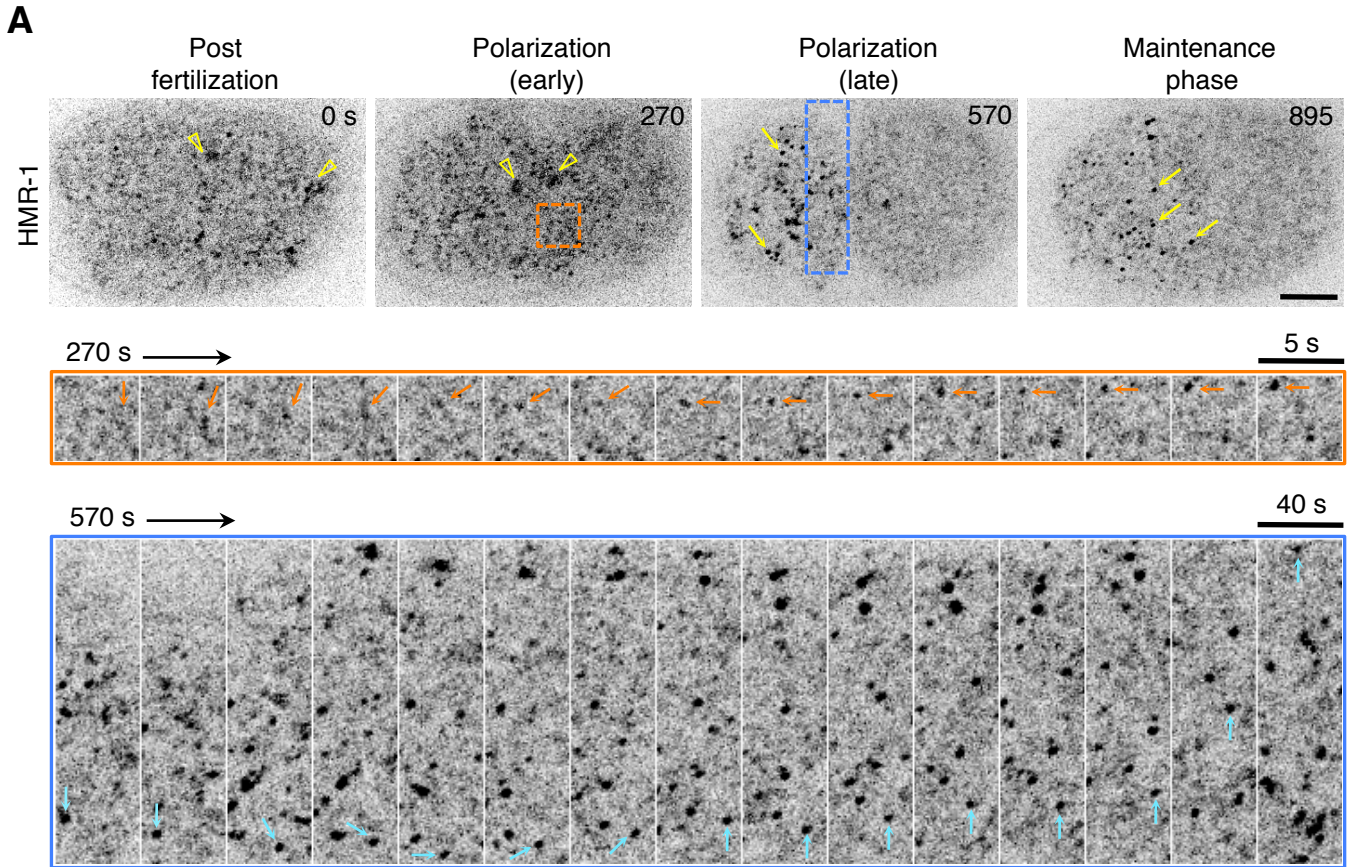


Figure S2

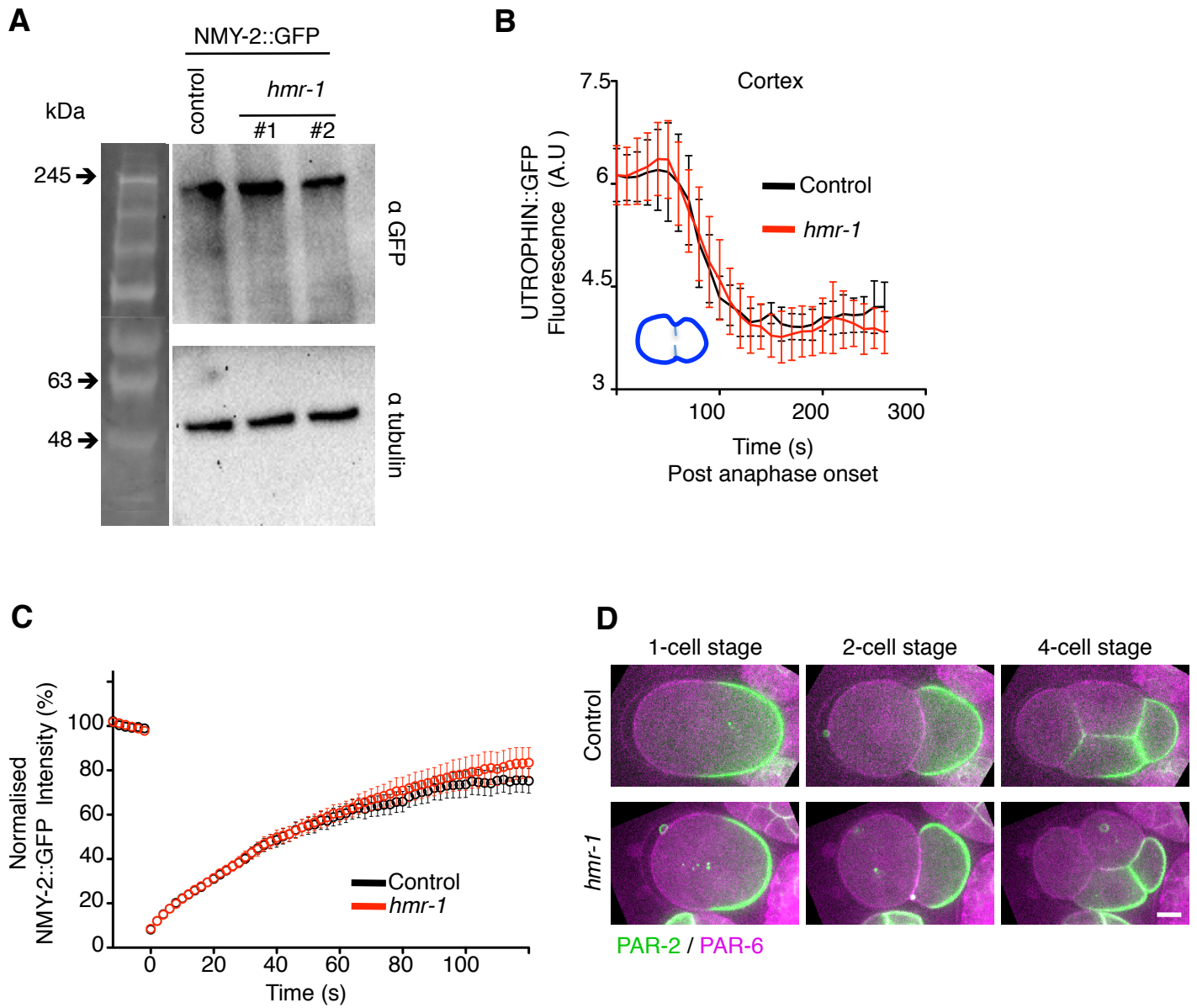


Figure S3

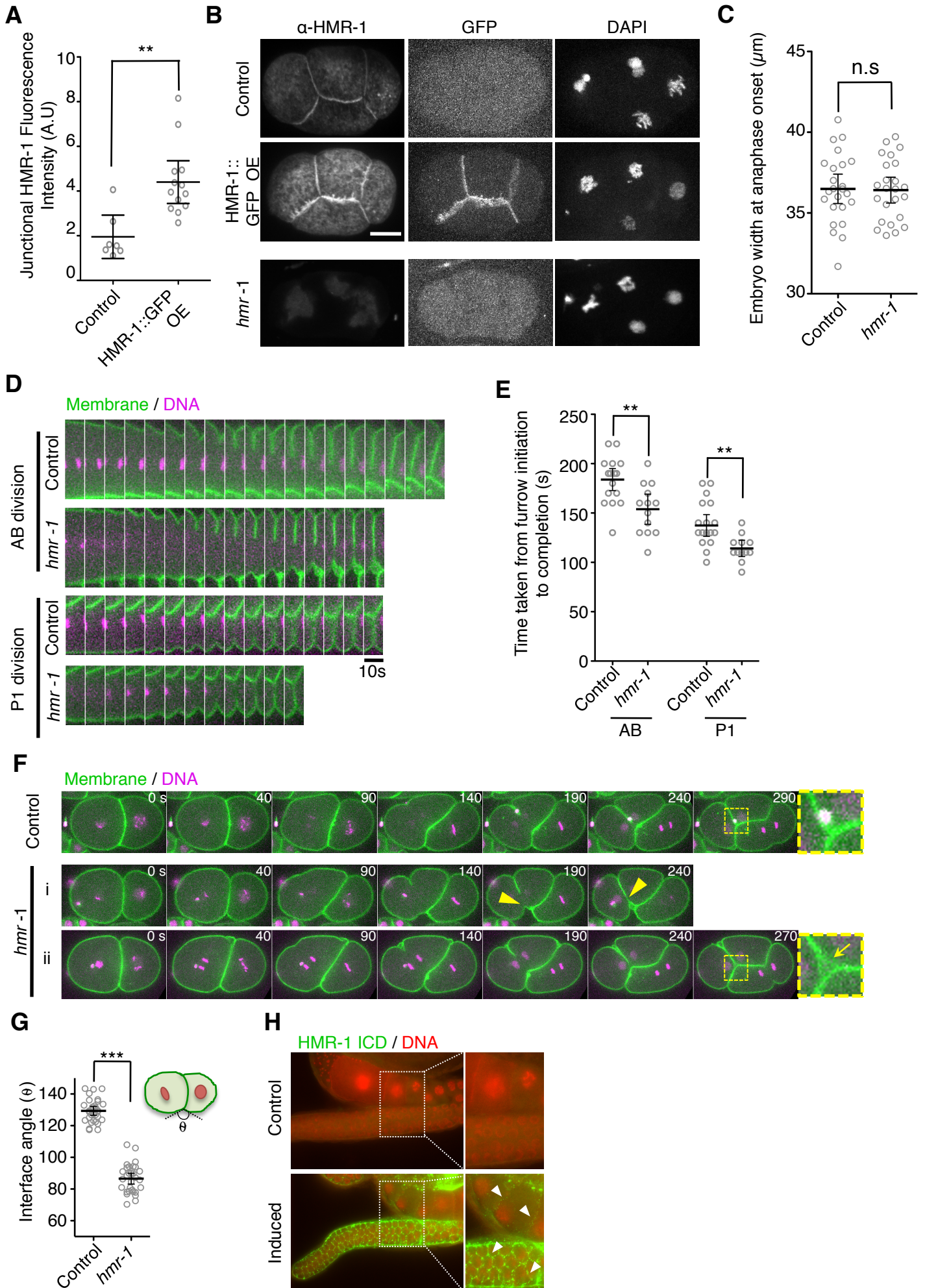
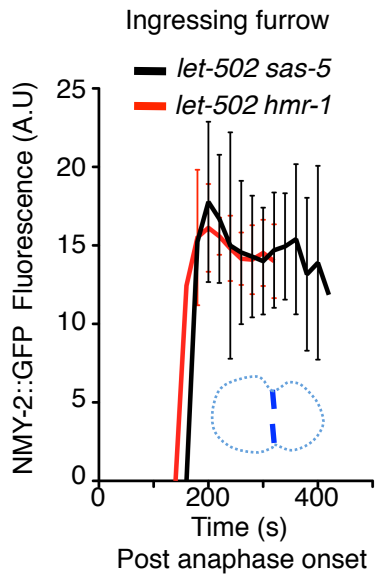


Figure S4



Supplemental figure legends:

Figure S1 (related to Figure 1). HMR-1 clusters assembled at non-junctional embryonic surface are stable and undergo actomyosin-dependent cortical movement (A) Cortical views of an embryo expressing HMR-1::GFP showing diffuse HMR-1::GFP (top panel, open yellow triangles) coalescing into well defined stable clusters (top panel, yellow arrows) during polarization. Enlarged orange region of interest (ROI) depicts the coalescence of diffuse HMR-1::GFP (middle, orange arrow) into a defined cluster. Enlarged blue ROI (bottom) shows the time series tracking the movement (cyan arrow) of the cluster assembled in the middle panel. HMR-1::GFP clusters assembled at a non-junctional surface are seen to be stable throughout the duration of image acquisition. See also Figure S1, Movie S1 and Movie S2. **(B)** Plot showing HMR-1::GFP levels measured at the surface of zygotes from post-fertilization till maintenance phase. Single cortical planes were imaged every 3 sec (n=5 embryos). Error bars denote mean \pm 95%CI **(C)** Cortical rotation is associated with cytokinesis initiation. Quantification showing the magnitudes of vertical component ($|V_Y|$, red curve, perpendicular to embryonic A-P axis) and horizontal component ($|V_X|$, green curve, parallel to embryonic A-P axis) of HMR-1::GFP cluster velocity and the kinetics of cytokinesis (blue curve) as measured by percentage of furrow ingression post anaphase onset in embryos expressing HMR-1::GFP mCherry::PH and Histone::mCherry (n=6 embryos). The maximum value of $|V_Y|$, $|V_Y|_{\max}$ coincides with the initiation of cytokinetic furrowing. $|V_X|$ and $|V_Y|_{\max}$ values shown are an average of 130 puncta from 6 embryos. Error bars denote mean \pm 95%CI. **(D)** Tukey plot showing $|V_Y|_{\max}$ and $|V_X|_{\max}$ values during cytokinesis in control (n=6 embryos) and *nmy-2 (ne3409)* (n=6 embryos) at 20 °C. (*p<0.05, Mann-Whitney U-test).

Figure S2 (related to Figure 2). Surface localized non-junctional HMR-1 negatively regulates cortical NMY-2 localization independent of F-actin and PAR complex (A) Western blot showing total NMY-2 levels in control and *hmr-1(RNAi)* worm lysates. The NMY-2 levels (normalized to loading control) from 2 independent experiments are 1.43 ± 0.2 and 1.22 ± 0.36 for control and *hmr-1(RNAi)* embryos, respectively **(B)** F-actin levels inferred from Lifeact::RFP intensity measured along the contact free surface in control (black curve) and *hmr-1(RNAi)* embryos (n=9) from anaphase onset (t=0 sec) till completion of furrow ingression. The level of F-actin at the cortex is not affected by HMR-1 depletion. Inset: the ROI measured is indicated in dark blue in the cartoon. **(C)** FRAP curves of NMY-2::GFP in a circular region of 25 pixel diameter in the anterior cortex of control and *hmr-1(RNAi)* embryos in maintenance phase showing similar recovery kinetics **(D)** Equatorial plane of GFP::PAR-2 and mCherry::PAR-6 in control and *hmr-1(RNAi)* embryos at 1-cell, 2-cell and 4-cell stages. Similar localization patterns of PAR proteins are seen in the presence or absence of HMR-1.

Figure S3 (related to Figure 3). HMR-1 regulation of cytokinesis is not limited to 1-cell embryonic stage. (A) Scatter plot showing the width at anaphase onset of control and *hmr-1(RNAi)* embryos. **(B)** Embryos from the indicated genotype were fixed and stained for HMR-1 (rabbit anti-HMR-1) and DNA (DAPI). GFP fluorescence was preserved in HMR-1::GFP OE strains post fixation. **(C)** Scatter plot showing total junctional HMR-1 levels in control and HMR-1 OE embryos. Junctional HMR-1 was measured by quantifying the fluorescence intensities of 5-pixel wide ROIs drawn along the cell-cell boundaries of embryos stained using α -HMR-1 antibody. Error bars are mean \pm 95%CI (**p<0.005, Mann-Whitney U-test) **(D)** Time lapse confocal images of the equatorial plane from divisions in AB and P1 cells in control and *hmr-1(RNAi)* embryos co-expressing GFP::PH and Histone::mCherry. The furrow takes a shorter time to complete ingression upon HMR-1 depletion. **(E)** Quantification for (C) showing faster furrow ingression in AB and P1 cells from *hmr-1(RNAi)* (n=13) than control (n=18) embryos. Error bars are mean \pm 95%CI (**p<0.005, Mann-Whitney U-test). **(F)** Timelapse series of equatorial planes showing division of AB cell in control and *hmr-1(RNAi)* embryos. Increase in cortical deformation due to loss of adhesion between AB and P1 cells upon HMR-1 depletion results in mispositioned furrow (arrowhead) and gaps between adjoining cells (arrow). **(G)** Plot showing the angle between the AB and P1 cells prior to anaphase onset in AB cell. **(H)** Immunofluorescence images showing expression of HA::PH::HMR-1-ICD in the germline (arrowhead) post heat shock induction.

Figure S4 (related to Figure 4) (A) Mean and 95%CI of NMY-2::GFP intensity measured along the ingressing furrow in *let-502;sas-5(RNAi)* (black curve, n=12) and *let-502;hmr-1(RNAi)* (red curve, n=14) embryos from anaphase onset (t=0 sec) till completion of furrow ingression. Inset: the ROI measured is indicated in dark blue in the cartoon.

Figure S4 (related to Figure 4) (A) Mean and 95%CI of NMY-2::GFP intensity measured along the ingressing furrow in *let-502;sas-5(RNAi)* (black curve, n=12) and *let-502;hmr-1(RNAi)* (red curve, n=14) embryos from anaphase onset (t=0 sec) till completion of furrow ingression. Inset: the ROI measured is indicated in dark blue in the cartoon.

Supplemental Experimental Procedures

Strains

The *C. elegans* strains used in this study are listed below.

Table of *C. elegans* strains used in this study

Strain	Genotype	Source	Reference
RZB135	<i>xnSi6 [mex-5P::HMR-1-GFP::hmr-1UTR]; zbls2(Ppie-1lifeACT::RFP)</i>	FT741 (Nance Lab) x BU70 (Bao Lab)	[S1, S2]
RZB81	<i>xnSi6 [mex-5P::HMR-1-GFP::hmr-1UTR]; zuls151[nmy-2::NMY-2::RFP + unc-119(+)]V</i>	FT741 x JJ1753 (Nance Lab, unpublished)	
RZB61	<i>unc-119(ed3) III; ltIs38 [pAA1; pie-1::mCherry::PH(PLC1delta1) + unc-119(+)]; ltIs44pAA173; [pie-1p-mCherry::PH(PLC1delta1) + unc-119(+)]; zuls45[nmy-2::NMY-2::GFP + unc-119(+)] V.</i>	OD183 (Oegema Lab) x RZB58	[S3]
RZB65	<i>unc-119(ed3) III ;xnSi6 [mex-5P::HMR-1-GFP::hmr-1UTR]; ltIs44pAA173; [pie-1p-mCherry::PH(PLC1delta1) + unc-119(+)]V; ltIs37 [(pAA64) pie-1p::mCherry::his-58 + unc-119(+)] IV</i>	RZB55 x RZB58	
MG589	<i>mgSi3[cb-UNC-119 (+) GFP::UTROPHIN]II</i>		[S4]
RZB134	<i>mgSi3[cb-UNC-119 (+) GFP::UTROPHIN]II; zuls151[nmy-2::RFP] ltIs37 [pie-1::mCherry::his-58 + unc-119(+)] IV</i>		
RZB58	<i>unc-119(ed3) III; ltIs38 [pAA1; pie-1::mCherry::PH(PLC1delta1) + unc-119(+)]; ltIs44pAA173; [pie-1p-mCherry::PH(PLC1delta1) + unc-119(+)].</i>	OD70 x OD95	[S5]
OD95	<i>unc-119(ed3) III; tIs37 [(pAA64) pie-1p::mCherry::his-58 + unc-119(+)] IV. ltIs38 [pAA1; pie-1::GFP::PH(PLC1delta1) + unc-119(+)]</i>	CGC	[S6]
RZB56	<i>nmy-2(ne3409) I unc-119(ed3) III ;xnSi6 [mex-5P::HMR-1-GFP::hmr-1UTR]; ltIs37 [(pAA64) pie-1p::mCherry::his-58 + unc-119(+)] IV</i>	WM179 (CGC) x RZB65	[S7]
JJ1473	<i>zuls45 [nmy-2::NMY-2::GFP + unc-119(+)] V</i>	CGC	[S7, S8]
LP162	<i>nmy-2(cp13[nmy-2::gfp + LoxP]) I.</i>	CGC	[S9]
MOT304	<i>unc-119 (ed3) III; mgSi5[cb-UNC-119 (+) GFP::ANI-1(AH+PH)] II; zbls2[Ppie-1lifeACT::RFP]</i>	Motegi Lab	[S2, S4]
TH414	<i>unc-119(ed3) III; par-2(ok1723); ddIs238[pie-1::GFP::par-2(CAI 0.26) + unc-119(+)]</i>	Hyman Lab	[S10]
RZB166	<i>xnEx384 [Phsp16::ha-phplc 1∂ 1 -hmr-1ICD pRF4; zbls2(Ppie-1lifeACT::RFP)ltIs37 [(pAA64) pie-1p::mCherry::his-58 + unc-119(+)] IV</i>	FT1568 (Nance Lab) X BU70 (Bao Lab)	[S2, S11]
RZB167	<i>xnEx385 [Phsp16::ha-phplc 1∂ 1 -hmr-1ICDm pRF4; zbls2(Ppie-1lifeACT::RFP)ltIs37 [(pAA64) pie-1p::mCherry::his-58 + unc-119(+)] IV</i>	FT1569 (Nance Lab) X BU70 (Bao Lab)	[S2, S11]
RZB248	<i>cyk-1 (knu83 C-terminal GFP, unc-119 (+)); unc-119(ed3) III; zbls2(Ppie-1lifeACT::RFP); ltIs37 (pie-1::mCherry::HIS-58)</i>	This study	

All strains were maintained on nematode growth medium (NGM) plates seeded with OP50 *E. coli*. All strains were grown at 20°C except RZB56 which was maintained at 15°C. Ectopic expression of PH-HMR-1^{ICD} was done as previously described in [S11] with slight modifications. Young adult worms with a single line of visible embryos were heat shocked at 34 °C for 90 minutes and allowed to recover for 3 hours at 20 °C to avoid the analysis of zygotes with any defects in meiosis or cytokinesis caused by the heat shock.

RNA interference (RNAi)

All RNAi experiments were done by microinjection of dsRNA, except for the Western blot analysis for NMY-2 (Figure S2A) for which RNAi via feeding was employed. Primers and templates used to amplify DNA templates for double stranded RNA (dsRNA) synthesis are indicated are tabulated below.

Table of Primers used to amplify templates used in dsRNA synthesis.

Gene	Primer 1	Primer 2	Template
<i>hmr-1</i>	taatacgaactactataggGAGTTCTA AGAGGCTCTGGGTG	taatacgaactactataggGTCCATTAT CATTACATCC	pJN455 (gift from Jeremy Nance)
<i>let-502, mel-11, gfp, sas-5</i>	CAGTCACGACGTTGTAAAC G	GCAACCTGGCTTATCGAAAT	ORF fragment cloned into L4440 feeding vector

Lower case denotes T7 sequences included for in-vitro dsRNA synthesis. Templates amplified from feeding clones used forward and reverse primers targeting regions in L4440 plasmid flanking the T7 sequences. In-vitro synthesized dsRNAs (Ambion MEGAscript RNAi Kit) were injected into L4 stage hermaphrodites at a concentration ~1 µg/ul using MINJ-1 microINJECTOR™ (Tritech Research, Inc, CA) and PatchMan™ NP2 micromanipulator (Eppendorf AG, Germany) mounted on a Nikon ECLIPSE Ti-S microscope. Hermaphrodites were dissected 36-48 hours post injection in M9 buffer and appropriate stage embryos were collected, mounted on 3% agarose pads and imaged. Remaining embryos dissected from the worms were collected on NGM plates to confirm *hmr-1* knockdown by visual observation of dead embryos.

The feeding construct used to for *hmr-1* knockdown in the western-blot analysis of NMY-2::GFP (Figure S2A) was a kind gift from Limor Broday (Tel-Aviv University). Feeding was carried out on plates as previously described [S12] with slight modifications. Embryos collected from gravid LP162 hermaphrodites were allowed to hatch and feed on the *hmr-1* RNAi plate at 25°C for 72-96 hours.

Worm lysis and western blotting

Equal numbers (~200) of worms from control (L4440) and *hmr-1* (RNAi) feeding plates were collected and washed 3x with (0.1%) PBS-Tween (PBST) followed by 1x wash with RIPA buffer containing protease inhibitors (Roche Complete protease inhibitor). The worms were then resuspended in ~20 ul RIPA buffer and flash frozen in liquid N₂. Subsequently, the samples were boiled in 2x Laemmli buffer containing 5% 2-mercaptoethanol for 5 minutes at 95°C, were centrifuged, and equal volumes of supernatant were loaded onto 4-20% Mini-PROTEAN Precast Gels (BIO-RAD) for immunoblot analysis. The proteins were then transferred to PVDF membrane and probed using the following antibodies: anti-GFP, 1:500 (Roche); anti-tubulin, 1:1,000 (Abcam ab18251). HRP-conjugated secondary antibodies: goat α-mouse (Abcam ab6789) ; rat anti-rabbit (Abcam ab102172) at 1:5,000).

Microscopy and Image acquisition

All imaging was carried out at 20°C on a Nikon-Ti microscope equipped with a 100x Plan-Apo 1.40 NA objective (Nikon, Tokyo, Japan) and CSU-X1 spinning-disk confocal head (Yokogawa Corporation, Tokyo, Japan). Focus drift during image acquisition was corrected using Nikon's Perfect Focus System (PFS). Embryo samples were excited using 491 and 568 nm DPSS-Laser (Roper Scientific, France) and images acquired using Evolve Rapid-Cal electron multiplying charged-coupled device camera (Photometrics, Tucson, AZ). Image acquisition was controlled by MetaMorph software (Molecular Devices, Sunnyvale, CA).

All images are single confocal planes (cortex or equatorial) acquired with the camera set at BIN1 except in Figure 2A and Figure S3D, where binning was set at 2x2.

Image Analysis

Image analysis and quantifications were carried out using Fiji, MATLAB and Microsoft Excel. Statistical analysis and graph plotting was carried out in Prism 6 software (GraphPad). Sample size and statistical tests used for individual experiments are detailed in corresponding figure legends.

Intensity line scan plot and co-localization analysis

To estimate the co-localization of cortical NMY-2::mCherry or Lifeact::RFP with HMR-1::GFP clusters, a 3 pixel wide and 20 pixel long (or 10 pixel long in Figure 2A) ROI was drawn with the cluster positioned at the center. Fluorescence intensities of both channels were measured along the ROI. Background intensity measured from an area outside the embryonic surface was subtracted from all pixels. For each embryo 9-15 ROIs were analyzed. To qualitatively analyze co-localization, a mean intensity profile was plotted for every embryo. Mean ± SEM intensities were plotted in Figure 1C(ii), and 2A from several embryos analyzed this way.

Quantitative analysis of the co-localization between HMR-1::GFP cluster and cortical F-actin during polarization, maintenance phase and cytokinesis was performed by calculating the Pearson's coefficient of correlation (PCC) between the two channels in every ROI. More than 100 PCCs were quantified per condition from 8-10.

Immunofluorescence

Immunolabelling of HMR-1 in embryos (Figure S3B), was done as described previously [S13]. Briefly, 6-8 gravid

hermaphrodites were dissected in 2 μ l H₂O on a poly-L-lysine (Sigma, P1524) coated glass slide. The embryos were cracked open on dry-ice, fixed (methanol -20°C, 15 mins) and permeabilized (0.05% PBS-Tween, 10 mins). Slides were incubated in 1:3 dilution of rabbit anti-HMR-1 (gift from Jeff Hardin, [S14]) primary antibody at 4°C overnight and subsequently at RT in 1:500 donkey anti-rabbit Alexa Fluor™ 568 (Life Technologies, A10042) secondary antibody.

For immunolabelling of HA::PH::HMR-1-ICD in the germline (Figure S3H), gonads isolated from worms dissected in PBS containing 0.2% Levamisole were fixed in 3% PFA, permeabilized in 0.1% PBS-Tween were stained overnight at 4°C in rabbit anti-HA primary antibody and subsequently in donkey anti-rabbit Alexa Fluor™ 488 (Life Technologies, A11008) secondary antibody at RT.

Fluorescence intensity measurements

To quantify the levels of NMY-2 in the cortex and cytokinetic furrow, a single confocal plane along the equator of embryos co-expressing NMY-2::GFP and mCherry::PLC1-PH was acquired every 10 seconds from anaphase onset. The image from the cell membrane channel was thresholded to generate a binary image of the cell boundary which was then used as a mask to measure fluorescence at the cell boundary in the background-subtracted NMY-2::GFP channel. To measure the intensity along the furrow or outer cortex independently, the mask was edited to include only furrow or only outer cortex ROIs. The above workflow was written into a Fiji macro and employed for our analysis.

The levels of F-actin were measured similarly with the exception that the F-actin image was used to create a mask for itself.

Fluorescence recovery after photobleaching (FRAP) analysis

FRAP experiments were performed with an iLAS2 module (Roper Scientific) on the spinning disk microscope described above. Cortical FRAP was carried out on a circular region of 25 pixel diameter at the anterior cortex of control and *hmr-1(RNAi)* embryos expressing NMY-2::GFP (LP162). Acquisitions were carried out at 1 frame per second. Recovery was measured in a circular ROI of 20-pixel diameter.

Analysis of cortical actomyosin and HMR-1 flow dynamics

To analyze the cortical F-actin flow and HMR-1 dynamics in the anterior region of embryos, single confocal planes of HMR-1::GFP and Lifeact::mCherry were acquired every 3s and analyzed using Particle Image Velocimetry (PIV). PIV analysis was performed using an open source MATLAB PIV toolbox, MatPIV 1.6.1 (<http://www.mn.uio.no/math/english/people/aca/jks/matpiv/>). Single-pass PIV with window size of 32x32 pixels and 50% overlapping windows was applied. Each velocity vector was resolved into components along the AP-axis, V_x and perpendicular to the AP-axis, V_y . $|V_x|$ and $|V_y|$ were estimated for each time point during cortical movement.

Tracking of HMR-1::GFP clusters or NMY-2::GFP foci was also performed manually using the ‘manual tracking’ plugin in Fiji. Single confocal cortical planes from embryos expressing HMR-1::GFP or NMY-2::GFP were acquired at defined time intervals (3s or 5s). The ‘X’ and ‘Y’ co-ordinates at each time point were used to calculate the magnitude of X and Y components ($|V_x|$ and $|V_y|$ respectively) of the instantaneous velocity of the tracked entity. For instance, if the cluster/focus moved from position 1 (x_t, y_t) to (x_{t+1}, y_{t+1}) over an acquisition time interval ΔT , for a BIN1 setting (1pixel= 0.16 μ m), the magnitude of the cluster/focus instantaneous velocity components was calculated using the formula $|V_x| = 0.16/\Delta T * (|X_{t+1} - X_t|)$ and $|V_y| = 0.16/\Delta T * (|Y_{t+1} - Y_t|)$. Calculated $|V_x|$ and $|V_y|$ values were plotted for each time point to obtain Figures S1C (red- $|V_y|$ and green- $|V_x|$) curves for HMR-1) and the maximum value of $|V_y|$ from such a curve (for NMY-2) was plotted as $|V_y|_{max}$ in Figure 4E.

Measurement of the kinetics of furrow ingression

Equatorial planes from control, *hmr-1(RNAi)* or HMR-1::GFP embryos co-expressing Histone::mCherry and mCherry::PH-PLC1 δ were acquired every 10 seconds post anaphase onset and the distance between the ingressing furrows was measured. This distance was normalized to the starting width and plotted as a function of time.

Supplemental References

- S1. Chihara, D., and Nance, J. (2012). An E-cadherin-mediated hitchhiking mechanism for *C. elegans* germ cell internalization during gastrulation. *Development* *139*, 2547-2556.
- S2. Huang, J., Wang, H., Chen, Y., Wang, X., and Zhang, H. (2012). Residual body removal during spermatogenesis in *C. elegans* requires genes that mediate cell corpse clearance. *Development* *139*, 4613-4622.
- S3. Carvalho, A., Desai, A., and Oegema, K. (2009). Structural memory in the contractile ring makes the duration of cytokinesis independent of cell size. *Cell* *137*, 926-937.
- S4. Tse, Y.C., Werner, M., Longhini, K.M., Labbe, J.C., Goldstein, B., and Glotzer, M. (2012). RhoA activation during polarization and cytokinesis of the early *Caenorhabditis elegans* embryo is differentially dependent on NOP-1 and CYK-4. *Mol Biol Cell* *23*, 4020-4031.
- S5. Kachur, T.M., Audhya, A., and Pilgrim, D.B. (2008). UNC-45 is required for NMY-2 contractile function in early embryonic polarity establishment and germline cellularization in *C. elegans*. *Dev Biol* *314*, 287-299.
- S6. McNally, K., Audhya, A., Oegema, K., and McNally, F.J. (2006). Katanin controls mitotic and meiotic spindle length. *J Cell Biol* *175*, 881-891.
- S7. Liu, J., Maduzia, L.L., Shirayama, M., and Mello, C.C. (2010). NMY-2 maintains cellular asymmetry and cell boundaries, and promotes a SRC-dependent asymmetric cell division. *Dev Biol* *339*, 366-373.
- S8. Nance, J., Munro, E.M., and Priess, J.R. (2003). *C. elegans* PAR-3 and PAR-6 are required for apicobasal asymmetries associated with cell adhesion and gastrulation. *Development* *130*, 5339-5350.
- S9. Dickinson, D.J., Ward, J.D., Reiner, D.J., and Goldstein, B. (2013). Engineering the *Caenorhabditis elegans* genome using Cas9-triggered homologous recombination. *Nat Methods* *10*, 1028-1034.
- S10. Goehring, N.W., Trong, P.K., Bois, J.S., Chowdhury, D., Nicola, E.M., Hyman, A.A., and Grill, S.W. (2011). Polarization of PAR proteins by advective triggering of a pattern-forming system. *Science* *334*, 1137-1141.
- S11. Klompstra, D., Anderson, D.C., Yeh, J.Y., Zilberman, Y., and Nance, J. (2015). An instructive role for *C. elegans* E-cadherin in translating cell contact cues into cortical polarity. *Nat Cell Biol* *17*, 726-735.
- S12. Hammell, C.M., and Hannon, G.J. (2012). Inducing RNAi in *C. elegans* by feeding with dsRNA-expressing *E. coli*. *Cold Spring Harb Protoc* *2012*.
- S13. Gonczy, P., Schnabel, H., Kaletta, T., Amores, A.D., Hyman, T., and Schnabel, R. (1999). Dissection of cell division processes in the one cell stage *Caenorhabditis elegans* embryo by mutational analysis. *J Cell Biol* *144*, 927-946.
- S14. Costa, M., Raich, W., Agbunag, C., Leung, B., Hardin, J., and Priess, J.R. (1998). A putative catenin-cadherin system mediates morphogenesis of the *Caenorhabditis elegans* embryo. *J Cell Biol* *141*, 297-308.